Research Article

Acoustic Emission Characteristics and Initiation Mechanism of Instantaneous Rock Burst for Beishan Granite

Chaosheng Wang [ID],[1,2] Hao Wan [ID],[1] Jianjun Ma [ID],[1,2] and Xianglin Chen [ID][1]

[1]*School of Civil Engineering and Architecture, Henan University of Science and Technology, Luoyang, Henan 471023, China*
[2]*Engineering Technology Research Center of Safety and Protection of Buildings of Henan Province, Luoyang, Henan 471023, China*

Correspondence should be addressed to Chaosheng Wang; 9905755@haust.edu.cn

In this paper, the instantaneous rock burst test of Beishan granite is carried out by using a deep rock burst simulation test system and an acoustic emission monitoring system. The acoustic emission data were monitored in real time during the test. The variation of the number and energy of acoustic emission events was studied, and the distribution characteristics of rock burst debris were analyzed. Based on plate and shell mechanics, the failure process of surrounding rock is discussed from the perspective of structural stability. The results show that (1) when the vertical stress reaches 171.31 MPa, the specimen is destroyed and the number of acoustic emission events and cumulative absolute energy before the specimen is destroyed increase sharply. (2) The debris generated by rock burst is mainly composed of slab debris, flaky debris, and thin flaky debris, accounting for 93.53% of the total debris. (3) When the length or height of the rock slab is constant, the maximum tensile stress in the rock slab decreases nonlinearly with the increase of rock slab thickness. For the same size of the rock slab, the farther away from the roadway wall, the greater the maximum tensile stress in the rock slab. (4) When the thickness of the rock slab is constant, the maximum tensile stress in the rock slab increases nonlinearly with the increase of height to thickness ratio K. When the ratio of height to thickness K is constant, the maximum tensile stress in the rock slab increases with the increase of rock slab thickness h. (5) With the increase of covering depth, the critical failure thickness of the rock slab decreases nonlinearly and the surplus energy increases nonlinearly.

1. Introduction

At present, China produces about 2000 tons of high-level radioactive waste every year. The storage of nuclear waste is close to saturation, and the demand for high-level radioactive waste disposal libraries is very urgent. Geological treatment of rock layers in deep underground areas is an internationally recognized method for proper disposal of high-level radioactive waste [1–3]. Many countries, such as France, Finland, Italy, and South Korea, have started to build underground nuclear waste repositories [4–11]. Granite has the characteristics of high strength and low permeability, so it has been selected by many countries as a potential bearing rock for the construction of underground nuclear waste

repository. In China, the Beishan area of Gansu Province is a large-scale granite underground, which has the advantages of good mechanical properties, stable geological structure, and less biological activity. After years of repeated assessment, the Beishan area has been identified as one of the best preselected sites for China's nuclear waste repository [12, 13]. However, when drilling exploration in the Beishan area, it is found that there is high ground stress in the local area, such as core cake phenomenon. The nuclear waste repository requires tens of thousands of years of safety, and the local high ground stress area is likely to induce rock burst during excavation unloading, which will not only affect the stability of the underground repository but also may pose a major threat to the construction of the underground

repository and the safety of the staff. Therefore, it is necessary to conduct in-depth research on the characteristics of rock burst and the initiation mechanism of Beishan granite.

Rock burst refers to a dynamic failure phenomenon caused by the instantaneous release of strain energy accumulated inside the rock due to excavation unloading under high ground stress conditions. At present, the definition of rock burst has not been unified. Cook [14] gave the definition of rock burst for the first time, that is, rock burst is the uncontrolled destruction of rock mass after the release of violent energy, while Russnes [15] believes that the new fracture surface of rock in the process of failure is accompanied by sound, spalling, spalling ejection, and other phenomena, which is rock burst. As the core of the research on rock burst, the mechanism of rock burst is related to the accuracy of rock burst prediction and the effectiveness of prevention and control measures. Therefore, it has become the focus of scholars at home and abroad. Chen et al. [16], based on uniaxial and triaxial rock tests under thermomechanical coupling, discussed the brittle failure mechanism of granite and evaluated the occurrence trend of rock burst at different temperatures. Based on the assumption of static and dynamic stress coupling, Cai et al. [17] studied the mechanism of rock burst and proposed four quantitative evaluation methods, which provided a method for understanding the mechanism of rock burst and monitoring rock burst. Based on a rock burst accident in a deep mine, Zheng et al. [18] analyzed the crack field, stress field, displacement field, and kinetic energy of roadway surrounding rock under cyclic dynamic load by using a particle discrete element method and discussed the instability mechanism of roadway rock burst roof. Si and Gong [19] conducted triaxial unloading compression tests on granite specimens to investigate the effects of the three-dimensional stress state and unloading rate on the rock burst mechanism. Tan et al. [20] established a mechanical model for energy release in surrounding rock of roadway, analyzed the law of energy release in surrounding rock of roadway, and revealed the mechanism of rock burst caused by kinetic energy release in surrounding rock. Gong et al. [21, 22] conducted true triaxial tests on granite and red sandstone cube samples containing prefabricated holes, reproduced the process of rock burst induced by spalling damage in deep-buried hard rock tunnels, and revealed the mechanism of rock burst induced by spalling damage. Based on the theory of slab deflection and energy principle, Guo et al. [23] established a mechanical model for roadway floor under high-level stress and studied the mechanism of rock burst in the floor of south track roadway in Xing'an Coal Mine.

Acoustic emission (AE) is a physical phenomenon in which part of strain energy is released as transient elastic wave under loading during crack propagation in rock. Because of its advantages of dynamic nondestructive monitoring and real-time analysis, it can record the whole process of rock failure. Therefore, many scholars have studied rock failure based on acoustic emission technology. Meng et al. [24] studied the energy accumulation, evolution, and dissipation characteristics of sandstone specimens during uniaxial cyclic loading and unloading compression at 6

different loading rates. The stress-strain relationship and acoustic emission characteristics of rock specimen deformation and failure are analyzed, and the law of energy evolution in the process of rock deformation and failure is revealed. Zhang et al. [25] conducted triaxial tests on granite specimens at a depth of 1150 m using an acoustic emission monitoring system to study the crack evolution and damage precursor characteristics during the deformation and damage process of deep granite under high peripheral pressure. Akdag et al. [26] studied the time-domain and frequency-domain response of strain rupture by using acoustic emission and kinetic energy analysis methods and quantified the thermal damage evolution process by the b value, cumulative acoustic emission energy, and event rate. Dong et al. [27] conducted tests on soft siltstone specimens under combined dynamic and static loads to quantitatively reveal the mechanical properties and acoustic emission characteristics of soft rock under different dynamic disturbances. Rasskazov et al. [28] proved a new method to solve the problem of local rock burst danger and rock burst prediction through acoustic measurement, spectrum correlation analysis based on acoustic emission signals, and the Griffith–Irwin [29, 30] fracture model. Moradian et al. [31] for a full understanding of the fracture process in brittle rocks tested prismatic specimens of granite containing preexisting flaws in uniaxial compression tests, and their cracking process was monitored with AE. The characteristics of the AE parameters and the evolution of cracking sequences were analyzed for every cracking level. Based on microcrack and macrocrack damage, a classification of cracking levels is introduced. Ren et al. [32] evaluated the temporal and spatial evolution and damage of microcracks in schist during true triaxial compression and strain rock burst tests using acoustic emission localization techniques and moment tensor analysis. Qin et al. [33] carried out three-point bending tests of sandstone under different spans, analyzed the acoustic emission characteristic parameters of sandstone fracture process, and obtained the damage evolution law of sandstone based on acoustic emission characteristics. Based on triaxial compression and acoustic emission tests, Wang et al. [34] studied the damage characteristics and mechanical properties of Beishan deep granite under different confining pressure levels and discussed the evolution of acoustic emission parameters and strain energy of deep rock at different damage stages.

In the investigation and study of hard rock failure, a large number of scholars have found that a large number of slab cracking failures exist, ranging from shear slip failure of geological faults to small rock specimens in laboratory tests [35, 36]. Slabbing failure, as a general rule and phenomenon of hard and brittle surrounding rock in deep-buried high-stress roadway, is shown as the surrounding rock cut by cracks approximately parallel to the excavation face, forming layers of thin slab approximately parallel to the excavation face [37]. It is generally believed that these rock slabs are the key to rock burst initiation. When the rock slab remains stable, the surrounding rock remains stable, while when the surface rock slab is suddenly unstable, the surrounding rock will spontaneously fail from the surface to the depth. At

present, the rock slab is often used to describe the failure phenomenon of rock burst or the initiation process of rock burst qualitatively. This paper intends to quantitatively describe the mechanical characteristics of rock burst initiation based on the failure of the rock slab.

In summary, scholars have conducted in-depth studies on the rock burst mechanism of different research objects, such as thermodynamic coupling, static and dynamic coupling, strength, and energy. However, there has been limited research on the initiation mechanisms of rock burst mechanics using structural stability theory. Extensive engineering practice has shown that slab structure failure is a common failure form of underground engineering surrounding rock. In view of this, this paper carried out an indoor instantaneous rock burst test on Beishan granite; during the test, acoustic emission data were monitored synchronously. The variation law of energy and acoustic emission events during the failure process of Beishan granite was studied, and the distribution characteristics of rock burst debris were analyzed. Based on plate shell mechanics, the initiation mechanisms of rock burst mechanics in Beishan granite were explored from the perspective of structural stability.

2. Test Conditions and Test Scheme

2.1. Test Conditions. Test rock samples were taken from the preselection area of Beishan, Gansu Province. The rocks were tonalite, complete, and fresh, and the samples were processed into cuboid specimens of 150 mm × 60 mm × 30 mm. The six surfaces of the specimen were highly polished to a flatness of 0.0025 mm per surface and a surface roughness of Raw 1.6.

Test equipment adopts the deep rock burst process simulation test system (Figure 1) independently developed by the China University of Mining and Technology (Beijing). The system has a test host, loading system, and data acquisition system. The acquisition system consists of a stress acquisition system, an acoustic emission acquisition system, and a camera system (Figure 2). The system can not only realize conventional tests such as uniaxial tension and compression, triaxial compression, tension and compression, tension, and shear but also realize true triaxial loading single-sided independent sudden unloading tests.

Stress acquisition uses a DSG9803 strain amplifier and a USB8516 portable data acquisition instrument, which can realize 8-channel independent acquisition. Acoustic emission adopts a PCI-II system provided by American Physical Acoustics Company. The acquisition frequency of AE sensors was set to 200 kHz, and the threshold value for signal acquisition was set to 26 dB. The amplification factor for signal acquisition was set to 40. A high-speed photography system can take and store images at a resolution of 1024 × 1024 at 1000 frames/s.

2.2. Test Scheme. The instantaneous rock burst test of Beishan granite specimens was carried out through laboratory tests to simulate the possibility of instantaneous rock burst in surrounding rock under different excavation depths.

FIGURE 1: Deep rock burst process simulation test system.

Because the mechanical properties of Beishan granite are stable and the texture is uniform, we carried out a rock burst simulation test on one specimen. As shown in Figure 3, the stress loading process is divided into three stages: in the first stage, at the beginning of the test, the specimen was initially loaded to the original stress corresponding to a burial depth of 500 m, that is, $\sigma_H = 15.14$ MPa, $\sigma_h = 10.57$ MPa, and $\sigma_v = 13.40$ MPa, and held for 5 minutes. According to the Kirsch equation, the excavation stress concentration is calculated; the vertical stress σ_V is 29.63 MPa after excavation along the minimum horizontal stress, and the whole process is recorded as level 1 loading. In the second stage, due to the small stress at this time, the possibility of instantaneous rock burst is less. To minimize the impact of continuous unloading on the rock properties, no unloading was performed under this stress state. After maintaining one stress state for 5 minutes, the next load is continued to be applied. Each level of loading is equivalent to an increase of 200 m in buried depth, and the whole process is 2 to 4 levels of loading in turn. In the third stage, when the burial depth increases to 1300 m, the original stresses are $\sigma_H = 32.74$ MPa, $\sigma_h = 23.37$ MPa, and $\sigma_v = 34.84$ MPa and the vertical stress σ_V is 81.15 MPa. This stress state had the potential to induce instantaneous rock burst, so instantaneous unloading was performed along the σ_h direction while keeping σ_H and σ_V constant to observe whether rock burst occurred. If rock burst occurs, the test is stopped; otherwise, the next level of load is applied, that is, $\sigma_H = 37.14$ MPa, $\sigma_h = 26.57$ MPa, and $\sigma_V = 94.03$ MPa. Then, it is unloaded instantaneously along the direction of σ_h, keeping σ_H and σ_V unchanged and observing whether rock burst occurs. If rock burst occurs, the test is stopped. If there is no rock burst, the next level of load is applied. The whole process is 5 to 12 levels of loading in turn. When the load reaches level 12, rock burst occurs, and the test is terminated.

3. Test Results and Analysis

3.1. Rock Burst Stress and Acoustic Emission Event Number Analysis. After multiple loading and unloading, when the original stress σ_v reaches 72.36 MPa, σ_H reaches 63.54 MPa,

1. Rock specimen

2. Loading pad plate

3. Pressure sensor

4. Loading rod

5. Removable loading lever

6. AE sensors

7. PAC AE monitoring system

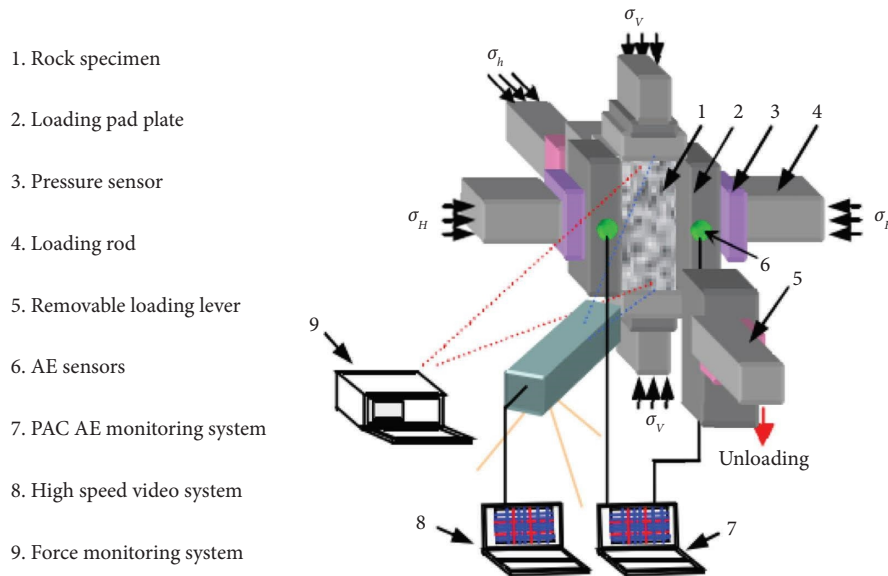8. High speed video system

9. Force monitoring system

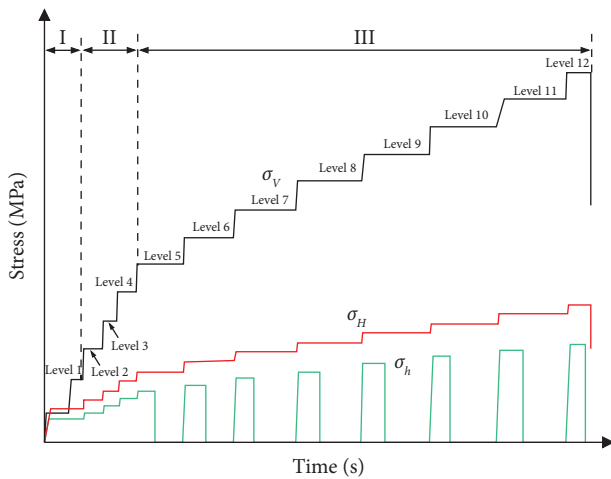Figure 2: Schematic diagram of the rock burst test system and monitoring system.

Figure 3: Stress-loading process diagram.

σ_h reaches 45.77 MPa, and the vertical stress σ_V is 171.31 MPa, the specimen has rock burst. At the moment of rock burst, the vertical stress σ_V dropped to 109.6 MPa and the horizontal stress σ_H dropped to 43.32 MPa. As shown in Figure 4, from the beginning of loading to the occurrence of rock burst, the generation of acoustic emission events is mainly concentrated in the unloading process of stage. During level 11, the number of acoustic emission events increases greatly and 1244 acoustic emission events are generated and with a slight crack sound, indicating that internal cracks of the specimen increase and crack propagation intensifies. During level 12, the number of acoustic emission events increases sharply and 13,855 acoustic emission events are generated in a short time, indicating that a large number of cracks expand, aggregate, and penetrate at this stage, which eventually leads to rock burst of the specimen with a violent noise.

The process of rock burst occurrence is shown in Figure 5. The failure process of the rock sample can be roughly divided into four stages: calm period, small particle ejection, flake stripping accompanied by particle mixing ejection, and recalm period. In the calm stage, as shown in Figure 5(a), the rock sample accumulates certain elastic strain energy through elastic deformation under loading. With the increase of σ_V, the initial microcracks in the rock sample develop and gradually converge to form larger cracks. Then, they enter the small particle ejection stage, and cracks transition from stable expansion to unstable expansion stage. Affected by material heterogeneity, several local fracture zones randomly form on the surface of the free surface, and the ejection of small particle cuttings occurs, as shown in Figure 5(b). In flake stripping accompanied by particle mixing ejection stage, the rock units in a certain depth range of the free surface are split under the action of compressive tensile cracking of σ_V, forming lamellar or plate-like rock slabs. With the continuous increase of σ_V, the rock slab on the surface of the free surface bulges and bends towards the free space, and stability gradually decreases. As shown in Figure 5(c), when σ_V increases to the peak strength of the rock sample, the rock slabs on the surface of the free surface will bend and break, and the residual elastic strain energy stored in the rock sample will be released sharply, forcing the broken thin rock slabs to eject quickly into free space, thus forming severe rock burst failure. Then, as shown in Figure 5(d), the rock sample returned to the calm period after experiencing severe rock burst.

3.2. Analysis of Acoustic Emission Energy Characteristics during Rock Burst. The change trend of the cumulative absolute energy of acoustic emission is basically the same as that of acoustic emission events; that is, there is an obvious increase when rock burst occurs, but the increase of absolute energy during destruction is more obvious than the number
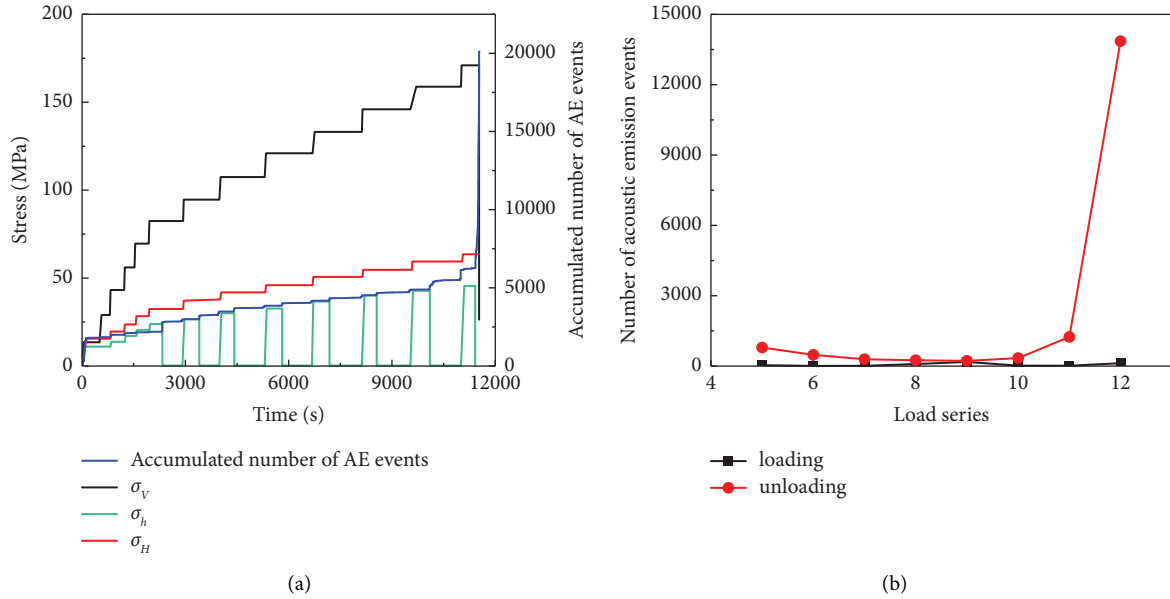
FIGURE 4: Variation of stress and acoustic emission events during the test. (a) Variation of stress and acoustic emission events over time; (b) the cumulative number of acoustic emission events varies with the loading series.

of acoustic emission events (Figure 6). Absolute energy is derived from the integral of the squared voltage signal divided by the reference resistance (10 k ohm) over the duration of the AE waveform packet. With the gradual loading of σ_V, the absolute acoustic emission energy increases slowly, the cumulative acoustic emission energy per level is small, and the average acoustic emission event energy is relatively low. When the load reaches level 12, the acoustic emission energy increases abruptly and the average acoustic emission energy increases sharply. At the moment of rock burst, multiple high-energy acoustic emission events are generated, indicating that large cracks expand rapidly at this stage, and rock burst occurs along with a violent sound.

3.3. Study on the Characteristics of Rock Burst Debris.

The macroscopic failure of rock is the result of continuous initiation, development, expansion, aggregation, and penetration of internal cracks. The debris after rock failure is the direct embodiment of fracture expansion, which reflects the fracture form and splitting process inside the rock. Therefore, it is necessary to analyze the geometric characteristics of rock burst debris. The categorization of rock burst debris is shown in Figure 7. According to the debris size, rock burst debris can be divided into four types: coarse debris, medium debris, fine debris, and microdebris. The particle size of coarse debris is larger than 30 mm, the particle size of medium debris is located in the range of 5–30 mm, the particle size of fine debris is located in the range of 0.075–5.00 mm, and the particle size of microdebris is smaller than 0.075 mm. Because it is difficult to obtain the geometric characteristics of debris with a small particle size, the debris with particle size greater than 5 mm is mainly studied, and the height (H), length (L), and thickness (T) of debris are measured by using a vernier caliper. According to

the height-to-thickness ratio of debris, the specimens were divided into four categories: block debris ($H/T < 3$), slab debris ($3 < H/T < 6$), flake debris ($6 < H/T < 9$), and thin flake debris ($H/T > 9$).

Figure 8 shows the distribution map of the debris size ratio of the specimen. The total amount of debris larger than 5 mm is 279, the maximum value of H/T is 16.92, the minimum value is 1.66, and the average value is 6.20. The maximum value of L/T is 10.16, the minimum value is 1.05, and the average value is 4.02. So, the characteristic size of $H/L/T$ is 6.20 : 4.02 : 1. The number of massive debris, tabular debris, flake debris, and thin flake debris is divided into 18, 135, 91, and 34, accounting for 6.47%, 48.56%, 32.73%, and 12.23% of the total. The debris is mainly composed of slab debris, flake debris, and thin flake debris, accounting for 93.53% of the total debris. For slab debris, flake debris, and thin flake debris, the maximum value of H/L is 16.92, the minimum value is 3, and the average value is 6.46; the maximum value of L/T is 10.16, the minimum value is 3.03, and the average value is 5.01; and the characteristic size of $H/L/T$ is 6.45 : 5.01 : 1. Considering the destruction of numerous sheet structures during the rock burst process, it is inferred that a substantial number of rock slabs had likely formed within the specimen's interior before rock burst occurred. The disruption of these rock slabs is highly likely to have triggered rock burst occurrence.

4. Study on Rock Burst Initiation Mechanism of Beishan Granite

4.1. Establishment and Solution of the Mechanical Calculation Model of Slabbing Failure.
In some typical deep hard rock projects at home and abroad, many scholars have observed tensile slabbing failure parallel to the excavation face in the engineering site (Figure 9). In addition, from the
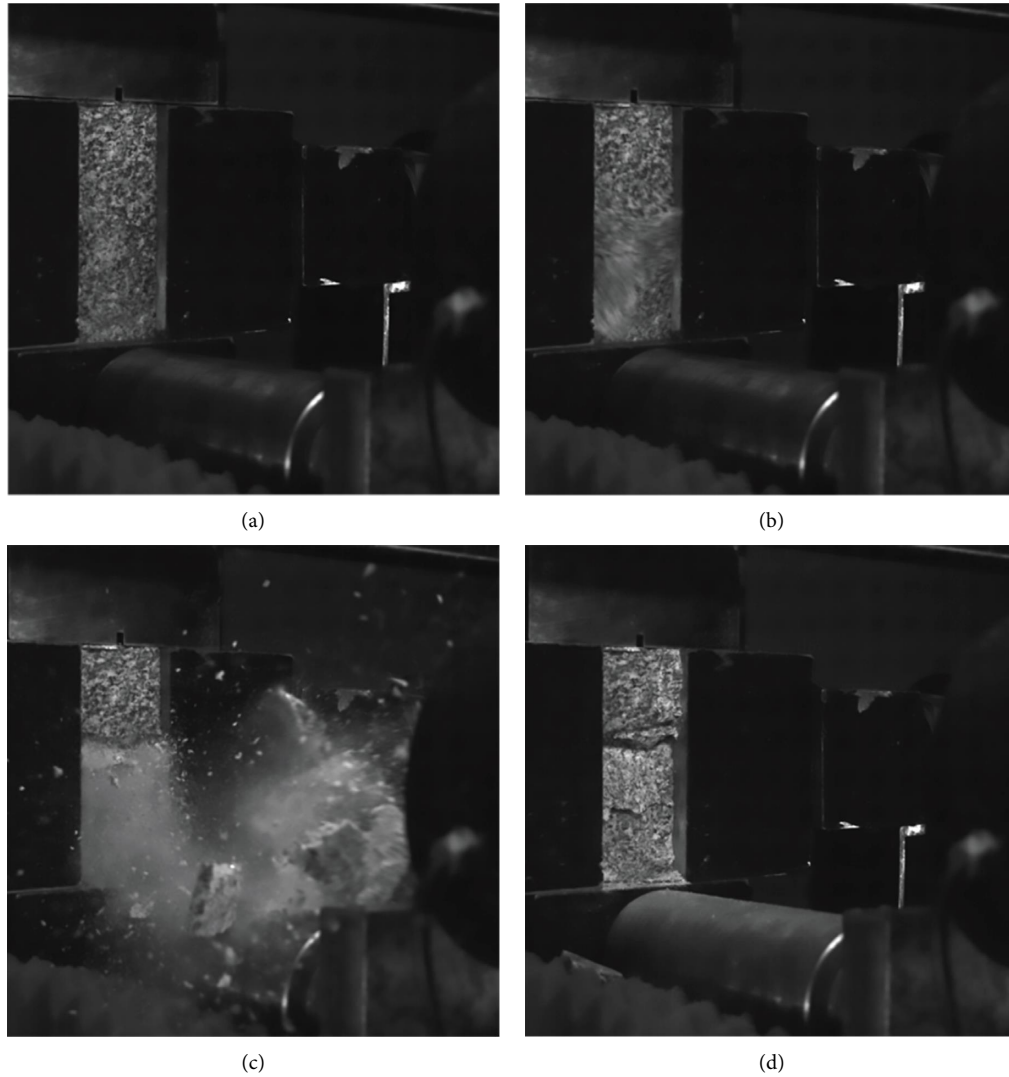
(a)

(b)

(c)

(d)

FIGURE 5: Schematic diagram of the rock burst process. (a) Calm stage; (b) small particle ejection stage; (c) flake stripping accompanied by particle mixing ejection stage; (d) recalm stage.

distribution of rock burst debris, it can be seen that the debris generated by the instantaneous rock burst test is also dominated by sheet structure. Considering that many slab structures are broken during the rock burst process, it is speculated that a large number of slab structures are formed inside the specimen before rock burst occurs. There is a strong correlation and essential connection between this slabbing phenomenon and rock burst. It can usually be considered as a precursory feature of strain-type rock burst in hard rock. Therefore, rock burst is likely to be caused by the destruction of these slab structures.

Assuming that a series of rock slab structures are formed inside the surrounding rock of the Beishan underground nuclear waste disposal repository, the stress distribution of the surrounding rock is shown in Figure 10. The surrounding rock forms a plastic bearing zone within a certain radius, and in the plastic bearing zone, both radial and tangential compressive stresses increase with the increase of radius and the tangential compressive stress reaches the

maximum value at the junction of the plastic bearing zone and the elastic bearing zone and then decreases with the increase of radius in the elastic bearing region, while the radial compressive stress keeps increasing with the increase of radius. Based on the stress distribution in the surrounding rock, it can be observed that both the tangential compressive stress and radial compressive stress encourage the rock slab structures to bend inward towards the interior of the roadway, resulting in unstable failure with ejection into the roadway's interior.

For ease of analysis and research, considering the effects of blasting and stress concentration, it is assumed that the plastic bearing zone radius of the roadway's surrounding rock is 1 m. Both the tangential compressive stress and radial compressive stress increase linearly. At the junction of the elastic bearing zone and the plastic bearing zone, the concentration factor for tangential stress is 2, while the concentration factor for radial stress is 0.5. After roadway excavation, it can be assumed that the surrounding rock
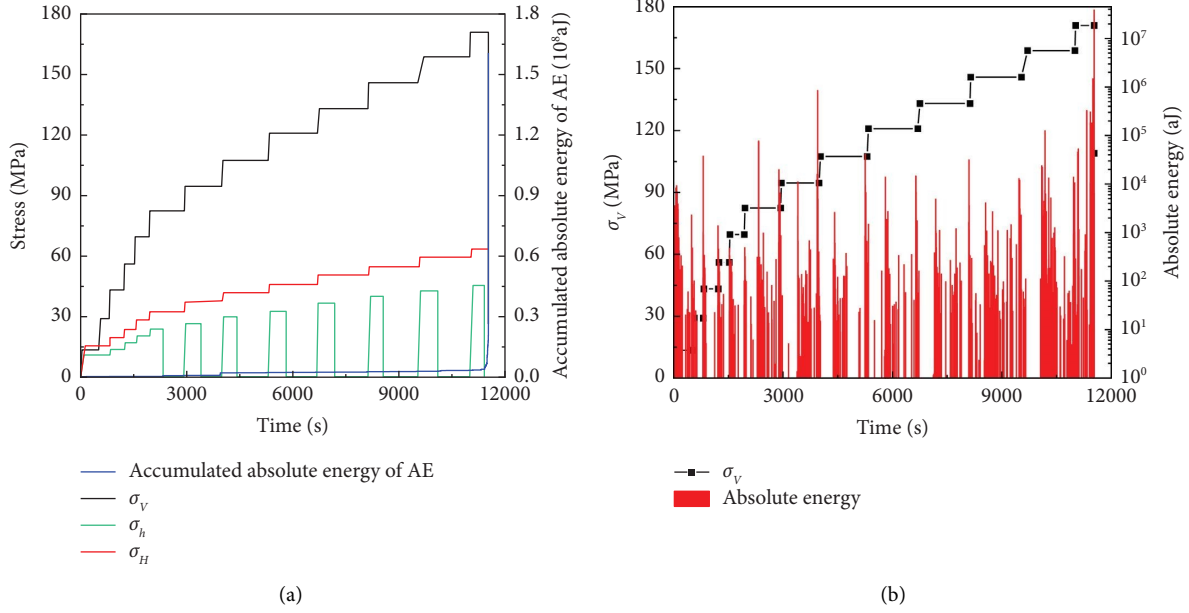
(a)

(b)

Figure 6: Variation of acoustic emission energy during the test. (a) The change in cumulative absolute energy of acoustic emission with time; (b) variation of acoustic emission event energy over time.
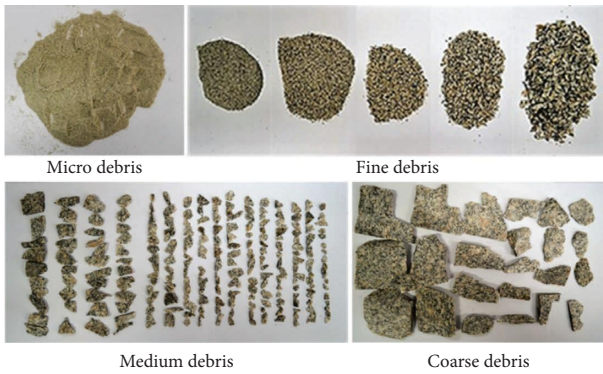

Figure 7: Classification of rock burst debris.

Figure 8: Distribution of geometric characteristics of specimen debris.

remains unchanged in strain along the direction of roadway advancement. Under the stress condition of a 500 m underground laboratory, $\sigma_v = 13.4$ MPa, $\sigma_H = 15.14$ MPa, and $\sigma_h = 10.57$ MPa, the analysis is carried out according to the plane stress-strain problem. The stress change equation in the plastic bearing zone is shown as follows:

$$\begin{cases} \sigma_1 = 26.80d, \\ \sigma_2 = 9.87 + 7.06d, \\ \sigma_3 = 5.29d. \end{cases} \tag{1}$$

In the equation, σ_1 is the tangential normal stress, σ_2 is the normal stress along the roadway, σ_3 is the radial stress, and d is the distance from the side of the roadway.

The stress condition and the calculation model of the rock slab formed by the surrounding rock are shown in Figure 11. If the length of the rock slab in the x direction is a, the length in the y direction is b, and the thickness is h, then
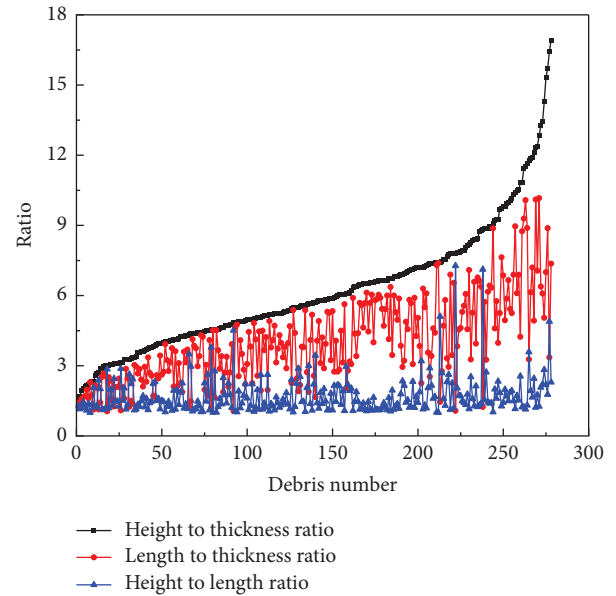
$$\begin{cases} F_x = (26.80d + 13.40h)bh, \\ F_y = (9.87 + 7.06d + 3.53h)ah, \\ M_x = 2.23bh^3, \\ M_y = 0.588ah^3, \\ q = 5.29h. \end{cases} \tag{2}$$

In the equation, M_x and F_x are the bending moment and pressure equivalent to the eccentric distribution stress on the upper and lower boundaries of the rock slab, M_y and F_y are

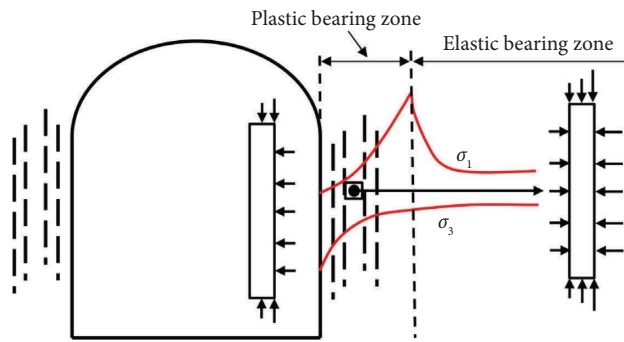FIGURE 9: Marble rock roadway failure diagram [35].

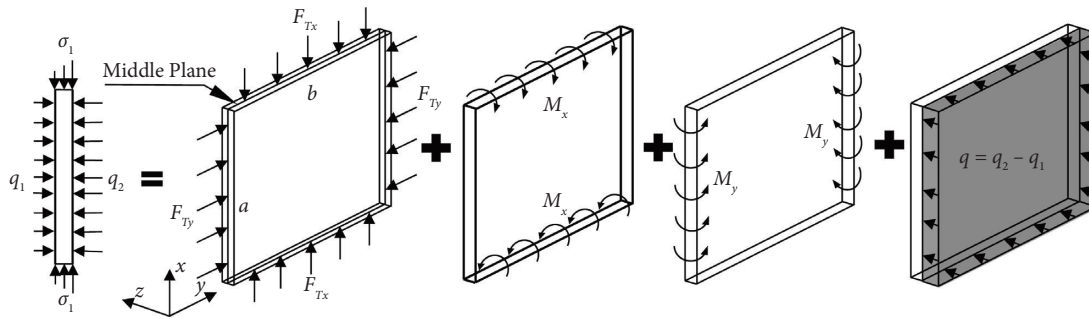FIGURE 10: Stress distribution diagram of surrounding rock.

FIGURE 11: Rock slab stress and calculation model.

the bending moment and pressure equivalent to the eccentric distribution stress on the left and right boundaries of the rock slab, and q is the lateral load difference on both sides of the rock slab.

For a four-sided simply supported thin slab, the boundary conditions are

$$w|_{x=0,a} = 0, \left.\frac{\partial^2 w}{\partial x^2}\right|_{x=0,a} = 0,$$

$$w|_{y=0,b} = 0, \left.\frac{\partial^2 w}{\partial y^2}\right|_{y=0,b} = 0. \tag{3}$$

The displacement satisfying the above boundary conditions can be taken as

$$w = \sum_{m=1}^{\infty}\sum_{n=1}^{\infty} A_{mn}\sin\frac{m\pi x}{a}\sin\frac{n\pi y}{b}. \tag{4}$$

The Rayleigh–Ritz method is used to calculate the deformation and stress of the rock slab. The increase of the deformation potential energy V_ε is

$$V_\varepsilon = \frac{D}{2}\iint_A \left(\nabla^2 w\right)^2 dxdy, \tag{5}$$

$$D = \frac{Eh^3}{12\left(1-\mu^2\right)}. \tag{6}$$

In the equation, D is the bending stiffness of the rock slab, E is the elastic modulus of the rock slab, and μ is Poisson's ratio.

The work done by the external load is

$$U = -\frac{F_{Tx}}{2}\iint_A \left(\frac{\partial w}{\partial x}\right)^2 dxdy - \frac{F_{Ty}}{2}\iint_A \left(\frac{\partial w}{\partial y}\right)^2 dxdy + \iint_A q(x,y)wdxdy + 2\int_{S_1} M_x\frac{\partial w}{\partial x}dS_1 + 2\int_{S_2} M_y\frac{\partial w}{\partial y}dS_2. \tag{7}$$

Substituting $F_{Tx} = -F_x$, $F_{Ty} = -F_y$, and $q(x,y) = q$ into (7), we obtain

$$U = \frac{F_x}{2}\iint_A \left(\frac{\partial w}{\partial x}\right)^2 dxdy + \frac{F_y}{2}\iint_A \left(\frac{\partial w}{\partial y}\right)^2 dxdy + \iint_A qwdxdy + 2\int_{S_1} M_x\frac{\partial w}{\partial x}dS_1 + 2\int_{S_2} M_y\frac{\partial w}{\partial y}dS_2. \tag{8}$$

On the upper and lower boundaries of the rock slab,

$$\int_{S_1} M_x\frac{\partial w}{\partial x}dS_1 = \sum_{m=1}^{\infty}\sum_{n=1}^{\infty} A_{mn}\frac{2M_x bm}{an}. \tag{9}$$

According to (5)–(8), the total energy of the system is

$$\int_{S_2} M_y\frac{\partial w}{\partial y}dS_2 = \sum_{m=1}^{\infty}\sum_{n=1}^{\infty} A_{mn}\frac{2M_y an}{mb}. \tag{10}$$

According to equations (5)–(8), the total energy of the system is

$$V_\varepsilon - U = \sum_{m=1}^{\infty}\sum_{n=1}^{\infty} A_{mn}^2\left[\frac{D\pi^4 ab}{8}\left(\frac{m^2}{a^2}+\frac{n^2}{b^2}\right)^2 - \frac{F_x\pi^2 m^2 b}{8a} - \frac{F_y\pi^2 n^2 a}{8b}\right] - \sum_{m=1}^{\infty}\sum_{n=1}^{\infty} A_{mn}\left(\frac{4qab}{mn\pi^2}+\frac{4M_x bm}{an}+\frac{4M_y an}{bm}\right). \tag{11}$$

For the equilibrium system, the partial derivative of the total potential energy to A_{mn} is 0:

$$\frac{\partial\left(V_\varepsilon - U\right)}{\partial A_{mn}} = 0. \tag{12}$$

From (11) and (12),

$$\sum_{m=1}^{\infty}\sum_{n=1}^{\infty} A_{mn} = \frac{\left(qab/mn\pi^2\right)+\left(M_x bm/an\right)+\left(M_y an/bm\right)}{\left[\left(D\pi^4 ab/16\right)\left(m^2/a^2+n^2/b^2\right)^2-\left(F_x\pi^2 m^2 b/16a\right)-\left(F_y\pi^2 n^2 a/16b\right)\right]}. \tag{13}$$

Substituting (13) into (4) yields

$$
w = \frac{\left(qab/mn\pi^2\right) + (M_x bm/an) + \left(M_y an/bm\right)}{\left[\left(D\pi^4 ab/16\right)\left(m^2/a^2 + n^2/b^2\right)^2 - \left(F_x \pi^2 m^2 b/16a\right) - \left(F_y \pi^2 n^2 a/16b\right)\right]} \sin\frac{m\pi x}{a}\sin\frac{n\pi y}{b}. \tag{14}
$$

The stress of each point in the rock slab is

$$
\sigma_x = -\frac{Ez}{1-\mu^2}\left(\frac{\partial^2 w}{\partial x^2} + \mu\frac{\partial^2 w}{\partial y^2}\right),
$$
$$
\sigma_y = -\frac{Ez}{1-\mu^2}\left(\frac{\partial^2 w}{\partial y^2} + \mu\frac{\partial^2 w}{\partial x^2}\right). \tag{15}
$$

Under the combined action of vertical and horizontal loads, along with lateral loads, rock slabs may experience two possible scenarios: tensile failure and compressive failure. According to (14) and (15), it can be seen that σ_x and σ_y take extreme values at ($a/2$, $b/2$, $h/2$) and ($a/2$, $b/2$, $-h/2$); that is, at the midpoint of the slab surface, the two sides of the slab will produce the maximum compressive stress and the maximum tensile stress. Since the compressive strength of granite is much greater than its tensile strength, the tensile stress is taken as the judgment basis in this paper, combined with the strength theory. If the following conditions are met, the rock slab will be destabilized and fail:

$$
[\sigma_t] \leq \sigma_{t,\max}. \tag{16}
$$

In the equation, $[\sigma_t]$ is the stress corresponding to when the rock slab reaches tensile strength and $\sigma_{t,\max}$ is the maximum tensile stress in the rock slab.

It is very important to consider the size effect when simulating instantaneous rock burst in the laboratory. The size of the test sample will affect the rock burst effect, dynamic response, stress and energy release, and other parameters. Selecting the appropriate sample size can simulate and analyze the characteristics and process of instantaneous rock burst more accurately and provide reliable test data and basis for the research and prevention of rock burst phenomenon. Since the assumption of a "thin plate" in elastic-plastic mechanics is followed when solving the force model of the rock slab, that is, the thickness (h) of the slab is less than 1/8~1/5 of the minimum size (a or b) in the middle plane. Therefore, in the following analysis of the influence of the rock slab shape such as the height, length, and height-to-thickness ratio on the internal stress of the rock slab, as well as the variation of the critical failure thickness and surplus energy with the buried depth of the rock slab, we also adopted the above assumption.

4.2. Analysis of the Influence of Rock Slab Height on the Internal Stress of Rock Slab.

Assuming that the maximum thickness of the rock slab is 0.2 m and the length of the rock slab is 1 m, according to (15), the variation trend of the maximum tensile stress within the rock slab with respect to the thickness of the rock slab can be calculated for rock slab heights of 0.6 m, 0.8 m, 1.0 m, 1.2 m, and 1.4 m. The rock slabs with $d = 0$, $d = 0.5$ m, and $d = 1.0$ m are selected to analyze the influence of the distance from the roadway wall on the stability of the rock slab (Figure 12). When the length of the rock slab is the same, the maximum tensile stress in the rock slab decreases significantly nonlinearly with the increase of the thickness of the rock slab, and the larger the height of the rock slab, the greater the maximum tensile stress in the rock slab. In addition, the maximum tensile stress in the rock slab increases with the increase of the distance from the roadway wall.

4.3. Analysis of the Influence of Rock Slab Length on the Internal Stress of Rock Slab.

Assuming that the maximum thickness of the rock slab is 0.2 m and the height of the rock slab is 1 m, according to (15), we can calculate the trend of the maximum tensile stress within the rock slab with respect to the thickness of the rock slab for rock slab lengths of 0.6 m, 0.8 m, 1.0 m, 1.2 m, and 1.4 m. The rock slabs with $d = 0$, $d = 0.5$ m, and $d = 1.0$ m are selected to analyze the influence of the distance from the roadway wall on the stability of the rock slab (Figure 13). It can be seen from Figure 13 that the variation trend of tensile stress inside the rock slab is the same as that in Figure 12. When the height of the rock slab is the same, it can be observed that the maximum tensile stress within the rock slab exhibits a significant nonlinear reduction as the thickness of the rock slab increases. Moreover, as the length of the rock slab increases, the maximum tensile stress within the rock slab also increases. In addition, for rock slabs of the same size, the maximum tensile stress within the rock slab increases with the distance from the roadway wall.

4.4. Analysis of the Influence of the Height-Thickness Ratio on the Internal Stress of Rock Slab.

The stress in the rock slab under different height-to-thickness ratios is calculated according to (15). The rock slabs with a length of 1.0 m and a thickness of 0.05 m, 0.1 m, and 0.15 m were selected to compare and analyze the change trend of stress. In addition, according to the assumption of elastic mechanics on thin slabs, rock slabs with height-to-thickness ratios K equal to 6, 7, 8, 9, and 10 are selected for stress analysis. The results are shown in Figure 14. When the thickness of the rock slab remains constant, it is evident that the maximum tensile stress within the rock slab nonlinearly increases with an increase in the height-to-thickness ratio K. Furthermore, for rock slabs of the same size, as the distance from the roadway wall decreases, the maximum tensile stress within the rock
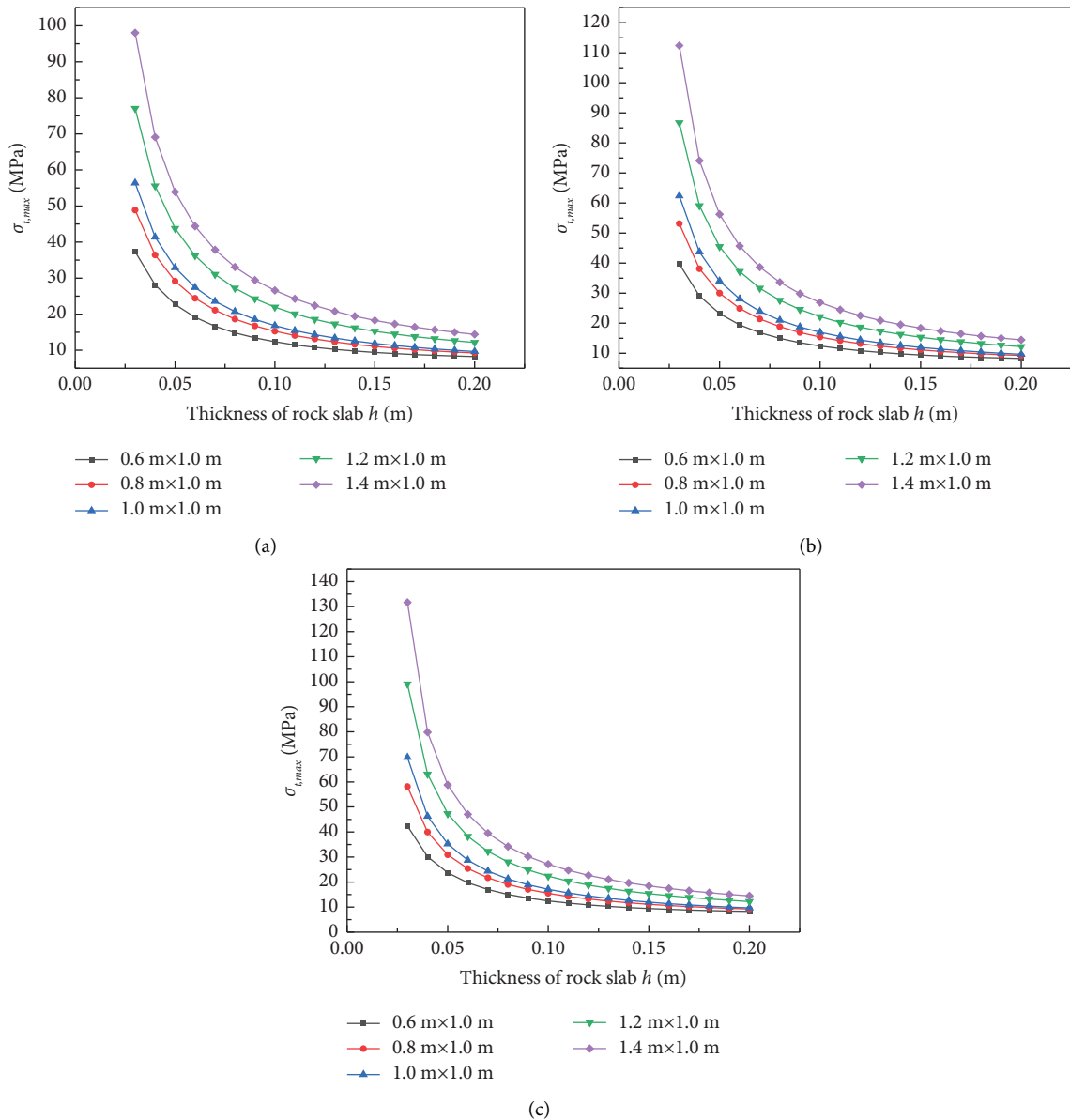
(a)

(b)

(c)

FIGURE 12: Variation of tensile stress with the thickness of rock slabs of different heights. (a) $d = 0$; (b) $d = 0.5$ m; (c) $d = 1.0$ m.

slab decreases, while it increases as the distance from the roadway wall increases. When the height-to-thickness ratio K is constant, as the thickness h of the rock slab increases, the maximum tensile stress within the rock slab also increases. Moreover, with increasing rock slab thickness h, the rate of stress increase becomes less steep. This occurs because thicker rock slabs have greater load-bearing capacity, experience less deformation, and have reduced bending stress's influence on overall stress.

4.5. The Change in Critical Failure Thickness and Surplus Energy with the Depth of Rock Slab.
The average characteristic size ($a/b/h = 6.45 : 5.01 : 1$) of the rock slab is selected to analyze the change in tensile stress with the thickness of the rock slab. As shown in Figure 15, with the increase of the thickness, the maximum tensile stress increases. When the thickness of the slab reaches a certain value, the maximum tensile stress may reach the tensile strength of the rock, leading to the failure of the rock slab. This thickness is
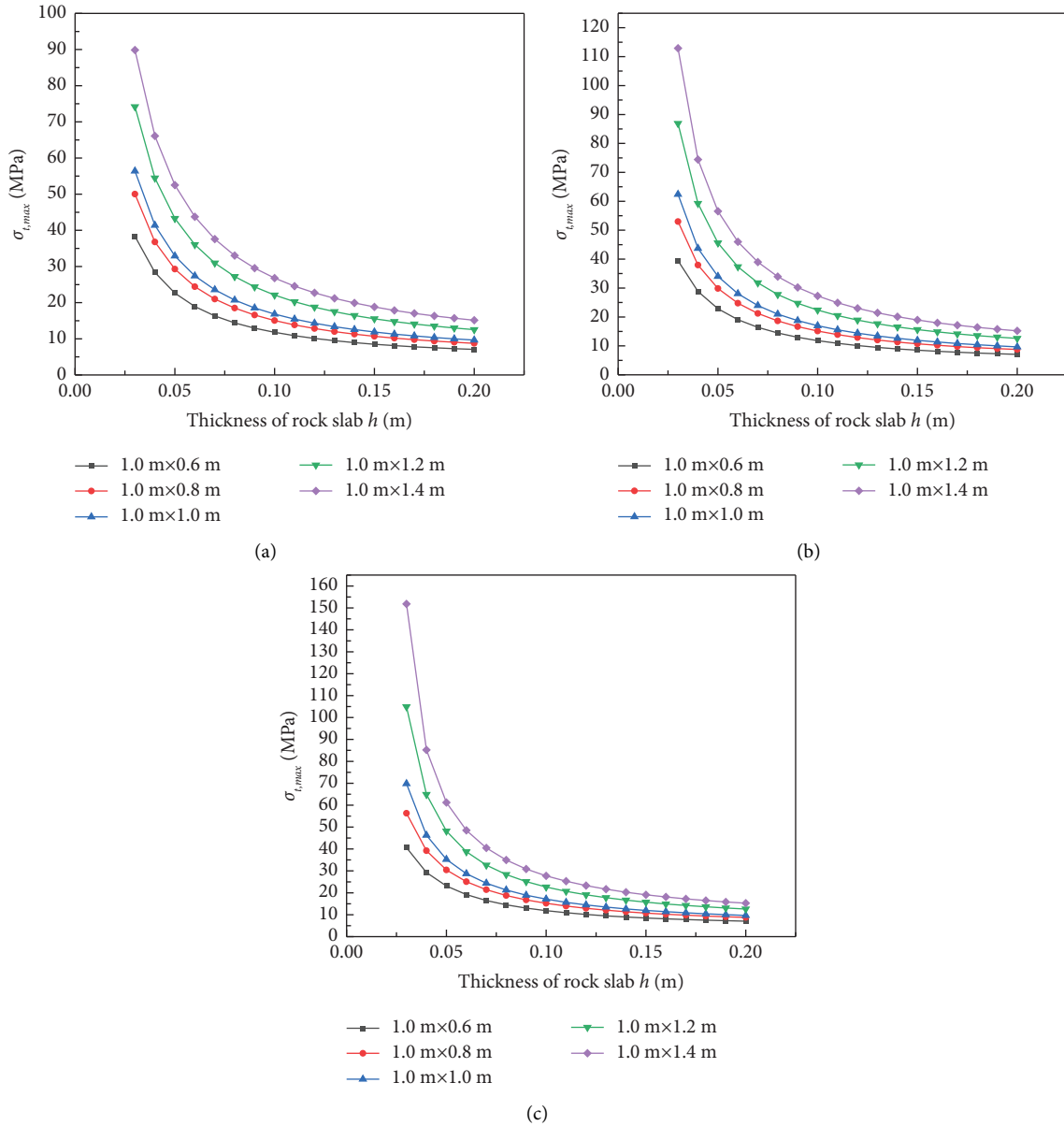
(a)

(b)

(c)

FIGURE 13: Variation of tensile stress of different lengths of slabs with thickness. (a) $d = 0$; (b) $d = 0.5$ m; (c) $d = 1.0$ m.

defined as the critical failure thickness h_{cr}. As the thickness of the rock slab is greater than h_{cr}, the rock slab is destroyed; otherwise, the rock slab remains stable. According to (14) and (15), h_{cr} is calculated with different depths (Figure 16). Further analysis shows that with the increase of depth, the critical failure thickness h_{cr} of the rock slab decreases from 0.1237 m to 0.0547 m, showing a nonlinear decrease, which indicates that in the case of a certain rock slab size ratio, the deeper the rock slab is, the more likely it is to be damaged.

Energy dissipation in the process of rock burst can reflect the intensity of rock burst. It is assumed that a series of rock slabs with a thickness of 0.15 m are formed in the surrounding rock ($a/b/h = 6.45 : 5.01 : 1$), and its energy is E_0. The energy corresponding to the critical failure thickness of the rock slab is defined as the critical failure energy E_{cr}. When E_0 is greater than E_{cr}, the rock slab will be destroyed, and furthermore, the difference between input energy and critical energy is defined as surplus energy. Surplus energy
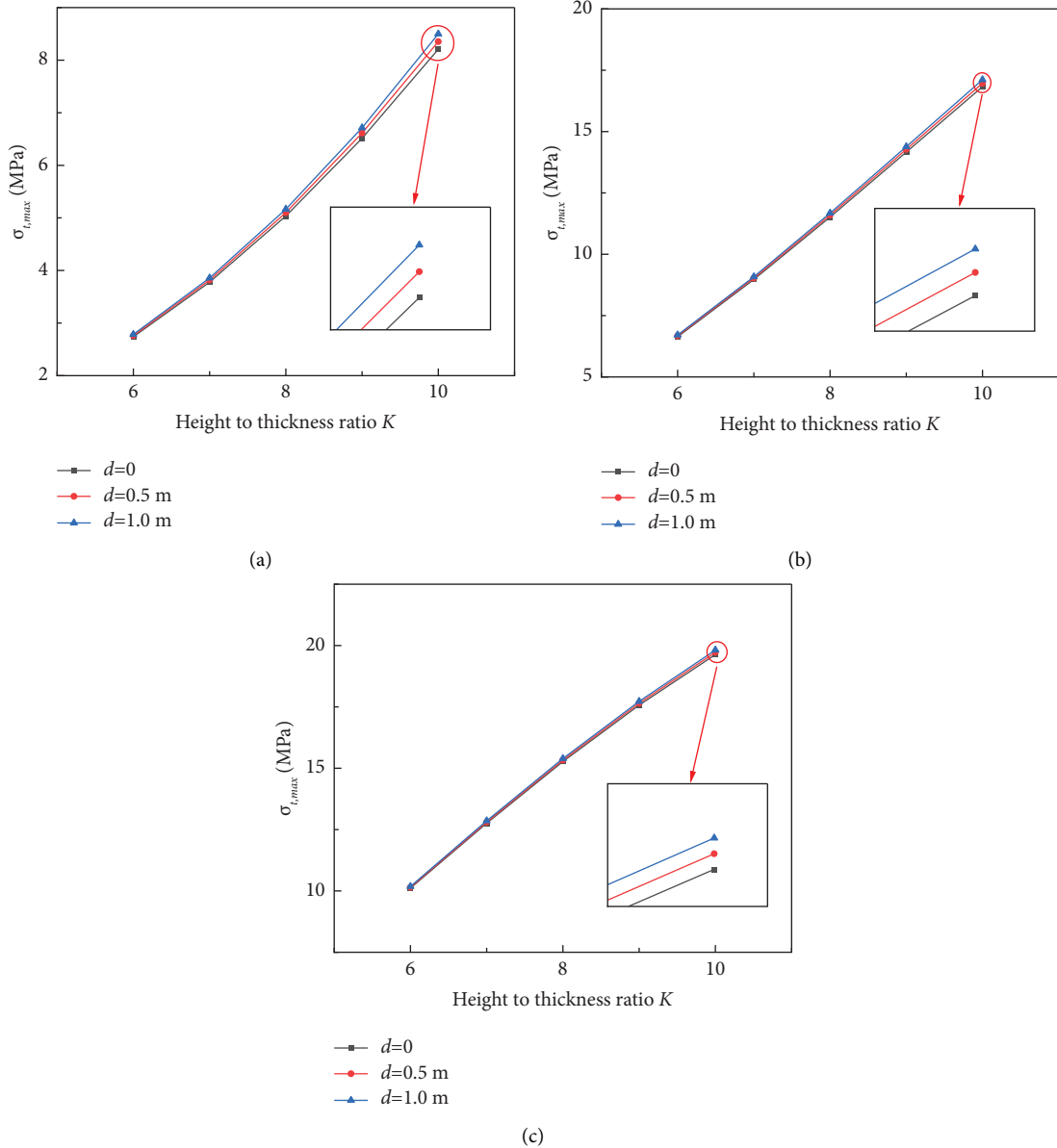
FIGURE 14: Stress variation of rock slab with different height-to-thickness ratios. (a) $h = 0.05$ m; (b) $h = 0.1$ m; (c) $h = 0.15$ m.

will be released in other forms (such as kinetic energy). The higher the surplus energy, the more severe the damage. Taking the energy E_0 as the reference object, the variation trend of the surplus energy of the rock slab at different depths is analyzed. As shown in Figure 16, with the increase of depth, the surplus energy increases from 8.61 J to 78.52 J, showing a nonlinear increase, which indicates that the same rock slab structure is more and more likely to be destroyed with the increase of depth, and the degree of damage is more and more serious.
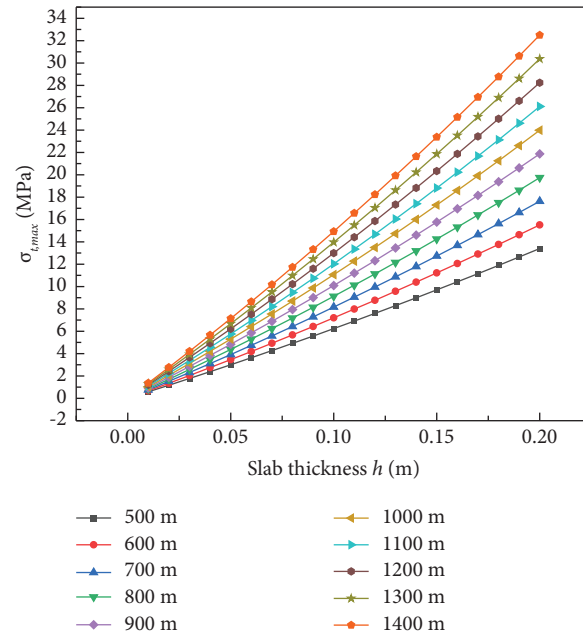
FIGURE 15: Variation of tensile stress with thickness for slabs with the same characteristic size.
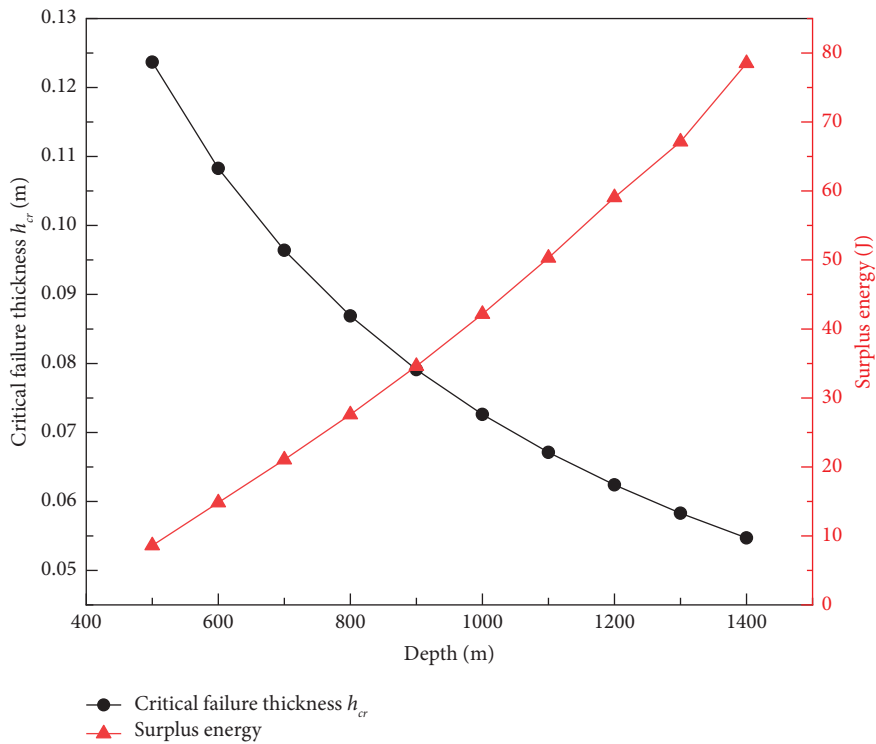

FIGURE 16: Variation of critical failure thickness and surplus energy with depth.

5. Conclusions

In this paper, we carried out an instantaneous rock burst test on the Beishan granite using the deep rock burst simulation test system. The variation law of the number of acoustic emission events and acoustic emission energy during the test was studied, the distribution characteristics of rock burst debris were analyzed, and the damage process of the surrounding rock from the perspective of structural stability was further explored preliminarily based on plate and shell mechanics. The research results can provide theoretical references for the construction and structural optimization of the Beishan underground nuclear waste repository and similar deep underground projects around the world. In addition, because the underground nuclear waste repository is still under construction, the stress distribution of the surrounding rock cannot be measured; therefore, when analyzing the damage process of the surrounding rock through the proposed model, the selection of parameters such as the radius of the plastic bearing zone and the stress concentration coefficient is different from the real stress of the surrounding rock of the underground experiments. Specifically, the following conclusions are obtained:

(1) When the vertical stress reaches 171.31 MPa, the specimen is destroyed, and the number of acoustic emission events and cumulative absolute energy before the specimen is destroyed increase sharply.

(2) The debris generated by rock burst is mainly composed of slab debris, flaky debris, and thin flaky debris, accounting for 93.53% of the total debris.

(3) When the length or height of the rock slab is constant, the maximum tensile stress in the rock slab decreases nonlinearly with the increase of rock slab thickness. For the same size of the rock slab, the farther away from the roadway wall, the greater the maximum tensile stress in the rock slab.

(4) When the thickness of the rock slab is constant, the maximum tensile stress in the rock slab increases nonlinearly with the increase of the height-to-thickness ratio K. When the ratio of height to thickness K is constant, the maximum tensile stress in the rock slab increases with the increase of rock slab thickness h.

(5) With the increase of covering depth, the critical failure thickness of the rock slab decreases nonlinearly, and the surplus energy increases nonlinearly.

Data Availability

The data used to support the findings of the study are available from the corresponding author upon request.

Conflicts of Interest

The authors declare that there are no conflicts of interest regarding the publication of this paper.

References

[1] J. Wang, L. Chen, R. Su, and X. G. Zhao, "The Beishan underground research laboratory for geological disposal of high-level radioactive waste in China: planning, site selection, site characterization and in situ tests," *Journal of Rock Mechanics and Geotechnical Engineering*, vol. 10, no. 3, pp. 411–435, 2018.

[2] P. Cook, "In situ pneumatic testing at Yucca Mountain," *International Journal of Rock Mechanics and Mining Sciences*, vol. 37, no. 1-2, pp. 357–367, 2000.

[3] Q. X. Lin, Y. M. Liu, L. G. Tham, C. A. Tang, P. K. K. Lee, and J. Wang, "Time-dependent strength degradation of granite," *International Journal of Rock Mechanics and Mining Sciences*, vol. 46, no. 7, pp. 1103–1114, 2009.

[4] C. Fairhurst, "Nuclear waste disposal and rock mechanics: contributions of the underground research laboratory (URL), pinawa, manitoba, Canada," *International Journal of Rock Mechanics and Mining Sciences*, vol. 41, no. 8, pp. 1221–1227, 2004.

[5] J. Delay, A. Vinsot, J.-M. Krieguer, H. Rebours, and G. Armand, "Making of the underground scientific experimental programme at the Meuse/Haute-Marne underground research laboratory, North Eastern France," *Physics and Chemistry of the Earth, Parts A/B/C*, vol. 32, no. 1-7, pp. 2–18, 2007.

[6] A. Brown, N. M. Soonawala, R. A. Everitt, and D. C. Kamineni, "Geology and geophysics of the underground research laboratory site, lac du Bonnet batholith, manitoba," *Canadian Journal of Earth Sciences*, vol. 26, no. 2, pp. 404–425, 1989.

[7] R. S. Read, "20 years of excavation response studies at AECL's Underground Research Laboratory," *International Journal of Rock Mechanics and Mining Sciences*, vol. 41, no. 8, pp. 1251–1275, 2004.

[8] J. B. Martino and N. A. Chandler, "Excavation-induced damage studies at the underground research laboratory," *International Journal of Rock Mechanics and Mining Sciences*, vol. 41, no. 8, pp. 1413–1426, 2004.

[9] T. Siren, M. Hakala, J. Valli, P. Kantia, J. A. Hudson, and E. Johansson, "In situ strength and failure mechanisms of migmatitic gneiss and pegmatitic granite at the nuclear waste disposal site in Olkiluoto, Western Finland," *International Journal of Rock Mechanics and Mining Sciences*, vol. 79, pp. 135–148, 2015.

[10] M. Souley, G. Armand, and J. B. Kazmierczak, "Hydro-elasto-viscoplastic modeling of a drift at the Meuse/Haute-Marne underground research laboratorory (URL)," *Computers and Geotechnics*, vol. 85, pp. 306–320, 2017.

[11] S. Kwon, W. J. Cho, and P. S. Han, "Concept development of an underground research tunnel for validating the Korean reference HLW disposal system," *Tunnelling and Underground Space Technology*, vol. 21, no. 2, pp. 203–217, 2006.

[12] X. G. Zhao, J. Wang, M. Cai et al., "In-situ stress measurements and regional stress field assessment of the Beishan area, China," *Engineering Geology*, vol. 163, pp. 26–40, 2013.

[13] L. Chen, C. P. Wang, J. F. Liu et al., "Damage and plastic deformation modeling of beishan granite under compressive stress conditions," *Rock Mechanics and Rock Engineering*, vol. 48, no. 4, pp. 1623–1633, 2015.

[14] N. G. W. Cook, "Seismicity associated with mining," *Engineering Geology*, vol. 10, no. 2-4, pp. 99–122, 1976.

[15] B. F. Russnes, "Analysis of rock spalling for tunnels in steep valley sides," M.Sc. thesis, Norwegian Institute of Technology, Trondheim, Norway.

[16] G. Q. Chen, T. B. Li, G. M. Li, C. A. Qin, and Y. H. He, "Influence of temperature on the brittle failure of granite in deep tunnels determined from triaxial unloading tests," *European Journal of Environmental and Civil Engineering*, vol. 22, no. sup1, pp. s269–s285, 2018.

[17] W. Cai, X. X. Bai, G. Y. Si, W. Z. Cao, S. Y. Gong, and L. M. Dou, "A monitoring investigation into rock burst mechanism based on the coupled theory of static and dynamic stresses," *Rock Mechanics and Rock Engineering*, vol. 53, no. 12, pp. 5451–5471, 2020.

[18] C. M. Zheng, J. Y. Zheng, X. J. Peng, and L. Zhou, "Study on failure characteristics and rock burst mechanism of roadway roof under cyclic dynamic load," *Shock and Vibration*, vol. 2021, Article ID 7074350, 11 pages, 2021.

[19] X. Si and F. Gong, "Strength-weakening effect and shear-tension failure mode transformation mechanism of rockburst for fine-grained granite under triaxial unloading compression," *International Journal of Rock Mechanics and Mining Sciences*, vol. 131, Article ID 104347, 2020.

[20] Y. Tan, W. Y. Guo, Y. L. Tan, T. B. Zhao, Y. X. Xiao, and Y. Chen, "Energy release law of roadway surrounding rock and energy-driven rock burst mechanism," *Journal of the Chinese Chemical Society*, vol. 46, pp. 609–620, 2021.

[21] F. Q. Gong, Y. Luo, X. B. Li, X. F. Si, and M. Tao, "Experimental simulation investigation on rockburst induced by spalling failure in deep circular tunnels," *Tunnelling and Underground Space Technology*, vol. 81, pp. 413–427, 2018.

[22] F. Q. Gong, X. F. Si, X. B. Li, and S. Y. Wang, "Experimental investigation of strain rockburst in circular caverns under deep three-dimensional high-stress conditions," *Rock Mechanics and Rock Engineering*, vol. 52, no. 5, pp. 1459–1474, 2019.

[23] D. M. Guo, X. C. Kang, Z. Y. Lu, and Q. Y. Chen, "Mechanism and control of roadway floor rock burst induced by high horizontal stress," *Shock and Vibration*, vol. 2021, Article ID 6745930, 13 pages, 2021.

[24] Q. Meng, M. Zhang, L. Han, H. Pu, and T. Nie, "Effects of acoustic emission and energy evolution of rock specimens under the uniaxial cyclic loading and unloading compression," *Rock Mechanics and Rock Engineering*, vol. 49, no. 10, pp. 3873–3886, 2016.

[25] L. Zhang, H. G. Ji, L. Y. Liu, and J. W. Zhao, "Time-frequency domain characteristics of acoustic emission signals and critical fracture precursor signals in the deep granite deformation process," *Applied Sciences*, vol. 11, no. 17, p. 8236, 2021.

[26] S. Akdag, M. Karakus, A. Taheri, G. Nguyen, and H. Manchao, "Effects of thermal damage on strain burst mechanism for brittle rocks under true-triaxial loading conditions," *Rock Mechanics and Rock Engineering*, vol. 51, no. 6, pp. 1657–1682, 2018.

[27] L. Dong, D. Wang, X. M. Sun et al., "Experimental study on the mechanical properties and acoustic emission characteristics of deep soft rocks under low-frequency dynamic disturbance," *Applied Sciences*, vol. 13, no. 11, p. 6399, 2023.

[28] I. Y. Rasskazov, S. V. Tsirel, A. O. Rozanov, A. A. Tereshkin, and A. V. Gladyr, "Application of acoustic measurement data to characterize initiation and development of disintegration focus in a rock mass," *Journal of Mining Science*, vol. 53, no. 2, pp. 224–231, 2017.

[29] A. A. Griffith, *Philosophical Transactions of the Royal Society A*, Royal Society, London, UK, 1920.

[30] G. Irwin, *Fracture of Metals*, ASM, Cleveland, OH, USA, 1948.

[31] Z. Moradian, H. H. Einstein, and G. Ballivy, "Detection of cracking levels in brittle rocks by parametric analysis of the acoustic emission signals," *Rock Mechanics and Rock Engineering*, vol. 49, no. 3, pp. 785–800, 2016.

[32] F. Q. Ren, C. Zhu, and M. C. He, "Moment tensor analysis of acoustic emissions for cracking mechanisms during schist strain burst," *Rock Mechanics and Rock Engineering*, vol. 53, no. 1, pp. 153–170, 2020.

[33] T. Qin, C. Jiang, Y. W. Duan, Y. W. Wang, and C. Ju, "Acoustic emission characteristics and damage evolution analysis of sandstone under three-point bending test," *Advances in Materials Science and Engineering*, vol. 2023, Article ID 9030449, 10 pages, 2023.

[34] C. L. Wang, G. Y. Du, Y. Han, K. He, and E. B. Li, "Evolution characteristics of acoustic emission and strain energy for deep granite under different damage stages," *Geomechanics and Geophysics for Geo-Energy and Geo-Resources*, vol. 9, no. 1, p. 14, 2023.

[35] W. D. Ortlepp, "The behaviour of tunnels at great depth under large static and dynamic pressures," *Tunnelling and Underground Space Technology*, vol. 16, no. 1, pp. 41–48, 2001.

[36] W. D. Ortlepp and T. R. Stacey, "Rockburst mechanisms in tunnels and shafts," *Tunnelling and Underground Space Technology*, vol. 9, no. 1, pp. 59–65, 1994.

[37] M. Cai, "Influence of intermediate principal stress on rock fracturing and strength near excavation boundaries-Insight from numerical modeling," *International Journal of Rock Mechanics and Mining Sciences*, vol. 45, no. 5, pp. 763–772, 2008.